Aerospace Science and Technology 160 (2025) 110026

Contents lists available at ScienceDirect

Aerospace Science and Technology

journal homepage: www.elsevier.com/locate/aescte

On flight instabilities of capsule-rigid parachute system during supersonic planetary descent

Luca Placco [a,*], Giulio Soldati [b], Matteo Bernardini [b], Francesco Picano [a,c]

[a] Centro di Ateneo di Studi e Attività Spaziali 'Giuseppe Colombo' (CISAS), Università degli Studi di Padova, via Venezia 15, Padova, 35131, Italy
[b] Department of Mechanical and Aerospace Engineering, Sapienza Università di Roma, via Eudossiana 18, Roma, 00184, Italy
[c] Department of Industrial Engineering, Università degli Studi di Padova, via Venezia 1, Padova, 35131, Italy

ARTICLE INFO

Communicated by Mehdi Ghoreyshi

Keywords:
Large eddy simulation
Supersonic parachute
Unsteady
Model
Mars exploration

ABSTRACT

High-fidelity time-evolving simulations of a rigid parachute trailing behind a descent module in a supersonic flight regime have been performed, employing Large-Eddy Simulation (LES) and Immersed-Boundary Method (IBM) techniques. The study aims to establish the fluid dynamic nature of the 'breathing' instability present also in a rigid decelerator, and thus its independence from structural flexibility. The turbulent wake of the descent capsule interacts with the bow shock generated by the parachute acting as the primary triggering factor. Energetic turbulent structures, accurately resolved by Large-Eddy Simulation, induce local fluctuations in the parachute shock, destabilizing its equilibrium with the upstream flow and leading to continuous cyclic motion of the shock wave. This motion correlates with periodic variations in flow pressure inside the canopy control volume, impacting parachute performance. Based on simulation results, a zero-dimensional model is developed to predict the unsteady dynamics of the shock motion and the decelerator performance. The model is driven by input fluctuations from the capsule wake, reproducing the main frequencies of shock position oscillations and drag variations as observed in simulations. It is apparent that unsteadiness is eventually triggered by low-frequency wake perturbations. Thus, the study provides insights into factors contributing to unsteady parachute responses in supersonic regimes.

1. Introduction

Aerodynamic decelerators have long been crucial to the success of planetary exploration missions. They serve as the primary means for achieving a feasible entry trajectory for space bodies with atmospheres. Ongoing research efforts are necessary to gain insights into their dynamics due to the evolving characteristics of spacecraft and the varying conditions associated with mission destinations, such as Mars or Venus. This requires a sturdy design process that can adapt to the diversity of various mission scenarios.

Although aerodynamic decelerators were developed in the previous century, they are still used today due to their simple manufacturing process and wide range of applications. While their initial technological advancements were driven by military applications, such as the introduction of vents to prevent oscillations, subsequent progress aimed at utilizing them specifically for planetary descent. Due to the unprecedented challenge, there were no existing examples of parachutes capable of operating in low-density environments at high speeds.

The first reported tests for developing parachutes for space applications come from Meyer [1], driven by the necessity of recovering missiles after launches [2]. Suffering from a legacy primarily of subsonic applications, there was no obvious decree which determined the correct way to find a suitable configuration; thus, trial and error represented the only alternative. For both configurations tested, towed and non-towed, violent pulsing of the canopy was observed; this is where the 'breathing' behavior was acknowledged for the first time. Variations in the shock pattern in front of the parachute were observed, but correlating them to specific operating conditions proved challenging due to limitations of the available equipment at the time. It was believed that the flexible nature of the device, combined with disturbances in the suspension lines, caused the erratic behavior.

The need for further testing was evident, especially with NASA's intention to adapt the technology for emerging space applications. In this

* Corresponding author.
E-mail address: luca.placco@unipd.it (L. Placco).

https://doi.org/10.1016/j.ast.2025.110026
Received 26 September 2024; Received in revised form 7 January 2025; Accepted 4 February 2025

Available online 6 February 2025

context, Maynard [3] investigated the performance of various types of drogue parachutes trailing behind a forebody in a wind tunnel. The focus was on decelerator stability and drag force, with consideration given to the role of Mach number and canopy porosity in determining the overall dynamics of the system and its suitability for the intended application. Once more, evident instabilities were observed. Despite the rigid canopy shape, asymmetrical shock patterns were detected in the parachute bow shock, resulting in unbalanced forces that could trigger an unstable response from the device.

Hence, the proper design and selection of a parachute opening at high speeds emerges as paramount. The parameters involved in building the device increase considerably, now encompassing not only the shape and dimensions of the decelerator but also its porosity and trailing distance. Simultaneously, alternative solutions aimed at reducing the ever-present instability emerged, including inflatables and cone-shaped decelerators [4,5]. However, their development halted as parachutes, with their longer legacy, proved sufficient for meeting the requirements of the first Mars exploration mission, namely the Viking program. Consequently, a particular design emerged from NASA contractors, demonstrating reliable performance in low-density environments: the Disk-Gap-Band (DGB) parachute [6]. This design would go on to become the current standard for descent trajectories.

Nonetheless, full-scale flight tests were still deemed necessary, prompting NASA to undertake a series of high-altitude supersonic parachute test programs between the 1960s and 70s [7–9]. These programs aimed to gain insights into the dynamics surrounding the device for application to Entry, Descent, and Landing (EDL), as well as explore plausible alternatives. The instabilities observed in wind tunnel tests were confirmed, along with an increase in the violence of oscillations as Mach numbers rose. Additionally, it was observed that the drag coefficient decreased at higher Mach numbers. Thus, a practical Mach number range was identified somewhere between 2.0 and 3.0, and the Disk-Gap-Band design was confirmed to be the best option. In particular, crucial parameters included also the relative dimension of the forebody producing the wake with respect to the decelerator diameter. An overview of the completed investigation campaigns was finally presented by Ross [10] and research established that these oscillations driving the unsteady dynamics were related to the wake developed by the forebody. The combination of these results obtained from previous wind tunnel testing and flight tests laid the groundwork for the Viking parachute system [11–13], which proved suitable after two successful landings on Mars (Viking I and II) [14].

All subsequent missions to Mars heavily relied on the Viking program, given the outstanding performance displayed by the device during the two previous entry trajectories. For the next 20 years, only small changes followed; alternative investigation approaches were limited primarily to the computational side, considering the limited resources available. In the 1970s, the first simulation methods based on gridless Vortex Element Methods (VEM) were proposed [15,16]: the distribution of bound vortex elements allowed the computation of flow around the decelerator, albeit limited to inviscid and incompressible flow cases, with no spontaneous account for unsteady phenomena and flow separation [17].

Refinements in the method allowed for coupling with structural models [18], providing promising results. However, the possibility of assisting experimental campaigns for future mission applications was considered distant, with the limitation to two-dimensional flows being one of the many issues at the time. Stein et al. [19] succeeded in simulating two-dimensional inflation profiles using an implemented Arbitrary Lagrangian-Eulerian (ALE) formulation coupled with a spring-damper structural model. ALE allows material to flow through the mesh as it deforms, varying its geometry. This approach was subsequently extended to three-dimensional flows [20], although tuning coefficients limited the analysis and comparison with experimental data was inconclusive. Further progress towards full three-dimensional simulations was achieved [21,22], but the study of flow unsteadiness was biased since the approaches were all based on steady-state solutions and the flow and structural solvers were handled separately (weakly coupled). It also became evident that a fine grid was essential to adequately resolve both the wake structure produced by the payload and the unsteady effects of interaction with the trailing canopy [17]. In addition, several models had to be properly coupled to represent the structural non-linear response, fabric porosity and suspension line tensions.

Consequently, the combined involvement of bluff and porous body aerodynamics, together with a nonlinear membrane structural response subjected to large deformations, all coupled to compressible flows possibly interacting with shock systems, delayed the breakthrough of computational approaches until the end of the 1990s.

Thus, conservatism and proper margin in the design allowed successive missions to Mars to rely on the heritage from the Viking era to qualify and deploy new parachute iterations successfully for the following decade (including the Mars Pathfinder, Mars Polar Lander, Mars Exploration Rover, and Phoenix missions) [23]. However, the limitation of this approach was evident as soon as it became necessary to step beyond the narrow boundary defined by the Viking legacy. With the Mars Science Laboratory (MSL) mission, adhering to the existing heritage was no longer feasible: the increased payload weight would subject the parachute to longer durations in supersonic flight, leading to multiple load cycles due to the ‘breathing’ phenomenon observed during the Viking-era tests, which were still partially understood. Additionally, the larger size of the parachute (the largest at the time) and the possibility of scale-dependent dynamic responses amplifying canopy oscillations necessitated a new supersonic parachute qualification process [24].

Since the costs associated with a full-scale test campaign were deemed prohibitive, sub-scale wind tunnel tests were complemented by validated computational fluid dynamics (CFD) and fluid-structure interaction (FSI) simulations for the very first time [25,26].

Barnhardt et al. [25] conducted a Detached-Eddy Simulation (DES) to investigate the aerodynamics of a rigid MSL parachute trailing behind the payload. The use of a fine grid, along with the unsteady solution of the flow field, revealed the generation of a highly turbulent wake from the descent module and its interaction with the parachute bow shock. This allowed the association of the parachute bow shock oscillation with the time-varying momentum deficit produced by the capsule wake. Furthermore, stronger fluctuations in the band region motivated the phenomenon of ‘area oscillation’ to be more driven by band movements.

Concurrently, Karagiozis et al. [26] pioneered the coupling of Large-Eddy Simulation (LES) with a Finite-Element Method (FEM) thin-shell-based structural solver capable of handling the overall Fluid-Structure Interaction dynamics of the ‘breathing’ instability post-inflation. The simulation reproduced canopy and drag oscillations, with limitations observed at higher Mach numbers where the treatment of suspension lines and models for sub-grid scale turbulence introduced sources of error. Most importantly, the study demonstrated how optimal turbulence resolution is crucial for observing shock motion and ‘area oscillations’, as these phenomena are completely absent at coarser grids.

This again emphasises the driving factor of instability on the fluid dynamics and highlights that proper wake representation is fundamental to accurately capture the transient responses of the decelerator.

Simultaneously with the MSL parachute development, ESA’s first Mars mission, ‘ExoMars’, was underway, and similarly, a parachute qualification program was initiated to study unsteady effects at supersonic regimes [27,28]. An ALE-LES fully coupled FSI approach discussed similar results regarding the effect of Mach number and forebody wake on parachute dynamics.

At that moment, with the breakthrough of CFD usage, multiple different approaches to the problem were proposed. Kim and Peskin [29] proposed an Immersed-Boundary Method (IBM) formulation applied to subsonic parachutes simulated for their entire descent. Takizawa et al. [30,31] developed a robust Fluid-Structure Interaction algorithm, which was applied to a comprehensive typology of parachutes in subsonic con-

ditions, modeling solid self-contact, canopy porosity, and suspension line effects.

Another notable example is the supersonic inflation sequence from a folded-line stretch configuration, which provided a time-evolution of the deforming structure of the parachute [32]. Muppidi et al. [33], in the framework of the latest full-scale test campaign ASPIRE for Mars2020 [34], investigated the wake effects from slender and bluff bodies, comparing DES results to flight tests at different angles-of-attack. Canopy-only dynamics were also evaluated, together with the differences between Earth's atmosphere and Mars'. These results led to further progress in the aerodynamic database of the mission [35]. In addition, LES was applied to study exclusively the entry capsule in supersonic flight, with the intent of characterising the turbulent wake flow produced by the blunt body, which eventually interacts with the trailing decelerator [36].

Progressively, the diffusion of High-Performance Computing (HPC) and the refinement of previous simulating solutions have led to the current state-of-the-art for supersonic parachute dynamics simulation, characterized by an extensive use of LES coupled to a solid solver, in various modalities. Yu and Pantano [37] further refined the previous approach adopted for the MSL computational study, replacing the interface treatment with an Immersed-Boundary Method approach. This allowed them to successfully simulate multiple cycles of canopy fluctuation in supersonic flight. The IBM algorithm has been recently updated to treat zero-thickness interfaces, although its application has been limited to simulating parachutes in subsonic flight [38].

LES coupled with a thin-shell based FEM solver via IBM was also employed, firstly by Huang et al. [39] and subsequently by Boustani et al. [40,41], to simulate the full supersonic deployment sequence and the subsequent cycles of oscillations of a DGB parachute. The simulation solutions were compared to flight test results, revealing a promising relation between the experimental data and the simulations.

To match the effective flight configuration as closely as possible, all of these computational methods employed modeling approaches to account for multi-physics phenomena that could affect the accuracy of the solution. These approaches ranged from turbulence modeling of the compressible turbulent flow to the dynamics on the structural side, including factors such as canopy porosity, self-contact effects and suspension lines shock interaction [42,43].

However, due to the extremely complex framework, simulations must be initialised properly to provide meaningful results [44,45]. Consequently, the stability boundary related to their initialisation appears to be narrow at the moment and possibly ill-conditioned. Moreover, with the now apparent wide variety of effects that could couple during parachute deployment, each deployment measured could be affected to a different extent by a diverse source, rendering comparison unfeasible due to statistical heterogeneity, even with all the current knowledge that has been collected. Additionally, the contribution of grid resolution sensitivity has yet to be fully assessed.

We believe that an intermediate approach could offer more insights into the overall phenomenon, with the ultimate goal of developing simplified models capable of describing the dynamics in its general aspect. Such models could aid the design process, which still heavily relies on empirical methods (e.g., the Mars Sample Return and the intended ASPIRE2 test campaign [46]).

As a result, the objective of this study is to provide a high-fidelity solution of the flow field surrounding a supersonic parachute trailing behind a descent capsule. The focus will be exclusively on the fluid-dependent sources of unsteadiness, demonstrating them to be the primary triggering factor of the so-called 'breathing' instability. Structure-dependent phenomena and effects will be ruled out, treating the geometry as rigid and minimising the introduction and influence of models within the simulation. The observed 'breathing' instability phenomenon is therefore solely attributed to the flow characteristics generated by the proposed system, emphasizing that the resulting fluid behavior is the only cause of the 'breathing' effect.

We utilize Large-Eddy Simulation to simulate a generic hemispheric parachute trailing behind a descent capsule (ExoMars-like), operating in the supersonic flight regime ($Ma_\infty = 2$) within the Martian atmosphere. To enable computation on a high-resolution grid, we leverage GPU parallelization. The resulting dataset is then analysed to accurately examine the flow behavior in the canopy region, focusing particularly on the interaction between shock waves and turbulence originating from the forebody wake. Special attention is paid to identifying the sources of unsteadiness that generate the dynamic behavior observed in the parachute bow shock. The data obtained from these simulations are ultimately used to develop a zero-dimensional model capable of providing semi-quantitative insights into the unsteady performance of the parachute during supersonic flight.

2. Governing equations and numerical methods

The three-dimensional filtered compressible Navier-Stokes equations are solved for a viscous Newtonian fluid:

$$\begin{cases} \dfrac{\partial \bar{\rho}}{\partial t} + \dfrac{\partial (\bar{\rho}\tilde{u}_j)}{\partial x_j} = 0 \\ \dfrac{\partial (\bar{\rho}\tilde{u}_i)}{\partial t} + \dfrac{\partial (\bar{\rho}\tilde{u}_i\tilde{u}_j)}{\partial x_j} = -\dfrac{\partial \bar{p}}{\partial x_i} + \dfrac{\partial \bar{\sigma}_{ij}}{\partial x_j} + \dfrac{\partial \sigma_{ij}^{SGS}}{\partial x_j} \\ \dfrac{\partial (\bar{\rho}\tilde{E})}{\partial t} + \dfrac{\partial (\bar{\rho}\tilde{E}\tilde{u}_j)}{\partial x_j} = -\dfrac{\partial (\bar{p}\tilde{u}_j)}{\partial x_j} + \dfrac{\partial}{\partial x_j}\left(\lambda \dfrac{\partial \tilde{T}}{\partial x_j} - q_j^{SGS}\right) \\ \quad + \dfrac{\partial}{\partial x_j}[(\bar{\sigma}_{ij} + \sigma_{ij}^{SGS})\tilde{u}_i] \end{cases} \tag{1}$$

where $\bar{\rho}$ is the filtered density, $\tilde{u}_i$ denotes the Favre-filtered velocity component in the ith Cartesian direction ($i = 1, 2, 3$), $\bar{p}$ is the filtered thermodynamic pressure. With the intent of reproducing the effect of Mars' atmosphere, the fluid is considered as an ideal gas of CO_2, with thermodynamic variables related by $\bar{p} = \bar{\rho} R \tilde{T}$, where $\tilde{T}$ is the Favre temperature and R is the gas constant. We denote with $\tilde{E} = c_v \tilde{T} + \widetilde{u_i u_i}/2$ the Favre-filtered total energy per unit mass and the dynamic viscosity $\mu(\tilde{T})$ is assumed to follow the generalised fluid power-law with exponent 0.76; the thermal conductivity λ is related to μ via the Prandtl number with the following expression: $\lambda = c_p \mu / Pr$. The ratio between the specific heat at constant pressure c_p and the specific heat at constant volume c_v is set to 1.3 while Prandtl number is 0.72.

The Favre-filtered viscous stress tensor $\bar{\sigma}_{ij}$ is expressed as:

$$\bar{\sigma}_{ij} = \mu\left(2\tilde{S_{ij}} - \frac{2}{3}\tilde{S}_{kk}\delta_{ij}\right) \tag{2}$$

$\tilde{S}_{ij}$ is resolved strain-rate tensor with $\tilde{S}_{ij} = 1/2(\tilde{g}_{ij} + \tilde{g}_{ji})$ and $\tilde{g}_{ij} = \partial \tilde{u}_i / \partial \tilde{x}_j$ is the resolved velocity gradient. The subgrid-scale (SGS) stress tensor σ_{ij}^{SGS} is modeled following Boussinesq's hypothesis as:

$$\sigma_{ij}^{SGS} = \mu_t\left(2\tilde{S_{ij}} - \frac{2}{3}\tilde{S}_{kk}\delta_{ij}\right) - \frac{2}{3}k^{SGS}\delta_{ij} \tag{3}$$

and the subgrid heat flux q_j^{SGS} is modeled from Fourier's law as:

$$q_j^{SGS} = -c_p \frac{\mu_t}{Pr_t}\frac{\partial \tilde{T}}{\partial x_j} \tag{4}$$

Subgrid-scale dynamic viscosity μ_t and the isotropic part k_{SGS} in the SGS stress tensor are modeled using a Wall-Adaptive Local Eddy-viscosity (WALE) model [47] modified via the Smagorinsky classical model [48]. We compute subgrid-scale dynamic viscosity as:

$$\mu_t = \bar{\rho}(C_w \Delta)^2 \frac{(S_{ij}^d S_{ij}^d)^{3/2}}{(S_{ij}S_{ij})^{5/2} + (S_{ij}^d S_{ij}^d)^{5/4}} \tag{5}$$

where $C_w = 0.325$ and $S_{ij}^d = 1/2(\tilde{g}_{il}\tilde{g}_{lj} + \tilde{g}_{jl}\tilde{g}_{li}) - 1/3(\tilde{g}_{ml}\tilde{g}_{lm}\delta_{ij})$; Δ is the local mesh size. By employing Yoshizawa's formulation [49] and using

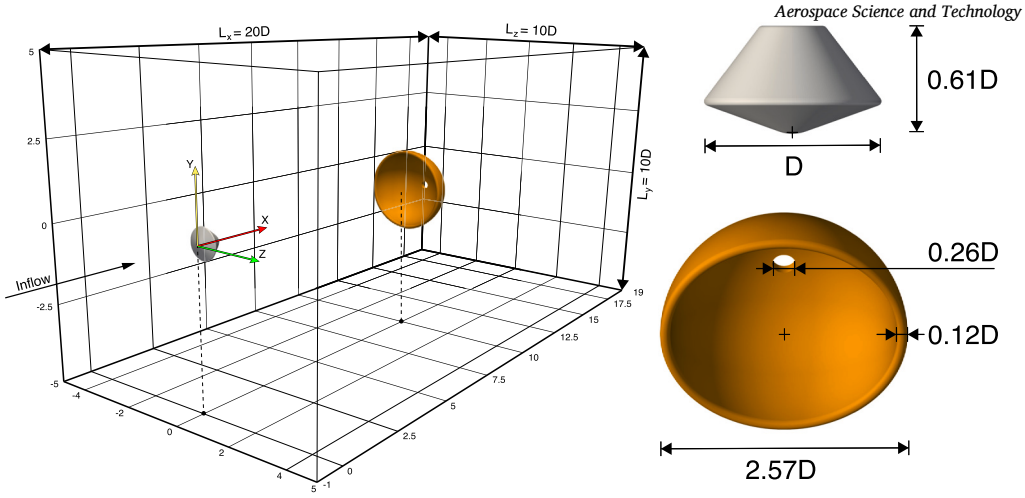

Fig. 1. Scheme of the computational domain (left) and visualization of the geometries of both the capsule and the parachute (right); dimensions are provided.

the coefficients of the Smagorinsky model, the isotropic part of the SGS stress tensor in eq. (3) can be computed as:

$$k^{SGS} = \frac{C_I'}{\tilde{\rho}} \left(\frac{\mu_t}{\Delta} \right)^2 \tag{6}$$

with C_I' found to be 45.8 [50]. The Prandtl turbulent number Pr_t is assumed equal to 0.9.

Flow equations (1) are numerically solved with the GPU-accelerated high-order finite difference solver STREAmS [51,52]. The solver is able to provide high-order and energy-preserving schemes to accurately discretise the convective terms of the equations in the shock-free regions. To account instead for flow discontinuities a Ducros shock sensor [53] is attached to high-order shock capturing WENO schemes to identify and solve flow regions affected from shocks. For the discretisation of the viscous terms, a locally conservative Laplacian formulation is used [54]. The present simulation employs a sixth-order scheme for the convective fluxes in shock-free regions, paired with a fifth-order WENO scheme for managing flow discontinutities; a sixth-order discretisation solves viscous terms. Time advancement of the ODE system is given by a third-order explicit Runge-Kutta/Wray algorithm.

The fluid/solid interface is handled using a ghost-point-forcing Immersed Boundary Method (IBM) [55] that can treat arbitrarily complex geometries. This method allows to pinpoint the grid nodes belonging to the fluid and to the solid, as well as their distance from the interface. No-slip and no-penetration wall boundary conditions on the body are then enforced by ghost nodes, which use interpolated values from the fluid domain to apply the local boundary condition on the solid. Further details of the algorithm can be found in [56]. Validation of the numerical solver for canonical flow cases and turbulent flows within similar regimes is documented in [57–59]. An additional test campaign featuring a sphere in multiple supersonic flow regimes is also included in Appendix B.

2.1. Description of the case

The domain employed for the simulation has a size of $L_x = 20D$, $L_y = 10D$, $L_z = 10D$, where $D = 3.8\,m$ is the maximum diameter of the capsule; the mesh is a rectilinear structured grid that consists of $N_x \cdot N_y \cdot N_z = 2560 \cdot 840 \cdot 840$ nodes which corresponds to the set of coordinates of $(x/D, y/D, z/D) = [-1, 19]\times[-5, 5]\times[-5, 5]$. A contraction factor of 0.2 is applied in the x direction, around the region of the canopy and the capsule, while a contraction of 0.3 is employed in the y, z direction, in the central portion of the domain.

Table 1
Simulation parameters.

Ratio of specific heats (γ)	1.3
Mach (Ma_∞)	2
Reynolds (Re_∞)	10^6
Prandtl (Pr)	0.72

Table 2
Free-stream reference values.

Pressure (P_∞)	265.11 Pa
Temperature (T_∞)	223.68 K
Density (ρ_∞)	$6.22 \cdot 10^{-3}$ Kg/m^3
Speed of sound (a_∞)	235.40 m/s
Viscosity (μ_∞)	$1.123 \cdot 10^{-5}$ $Pa \cdot s$

This allows to increase grid density in the surrounding space of the capsule and the canopy, improving flow resolution near the wall and in the wake area, where turbulent production is expected. The entry capsule is fixed at the position [0,0,0] (nose) while parachute trailing position has been set to [10,0,0]. This value was selected as inbetween to the previous ExoMars 2016 mission and the upcoming 'Rosalind Franklin' in order to highlight the effects of interaction between capsule and parachute.

Capsule geometry has been modeled on the specifications of ExoMars 'Rosalind Franklin' module, while the rigid parachute employs the basic shape of an hemisphere. Parachute nominal diameter is $D_0 = 15m$ and has been selected equal to the diameter of the supersonic decelerator foreseen the 'Rosalind Franklin' mission. Considering the typical inflation ratio for a DGB of $D_p/D_0 = 0.65$, the non-dimensional diameter of the canopy is $D_p = 2.57D$. The non-dimensional diameter of the vent and the canopy thickness are respectively set to $D_v = 0.26D$ and $t_p = 0.12D$. Domain and models details have been reported also in Fig. 1.

Flow condition and reference free-stream values are reported in Table 1 and 2, and are selected to match the full inflated state of the parachute deployment sequence after line-stretch, assuming that the oscillations produced by the inflation are already damped. The fluid properties have been obtained using a simulated entry and descent trajectory of a generic probe through the Mars atmosphere [60]. The Reynolds number is computed as $Re_\infty = \rho_\infty U_\infty D/\mu_\infty$ with μ_∞ being the flow dynamic viscosity and $Ma_\infty = U_\infty/a_\infty$.

Computations have been carried out on CINECA's Leonardo Booster cluster, using a total of 64 GPUs.

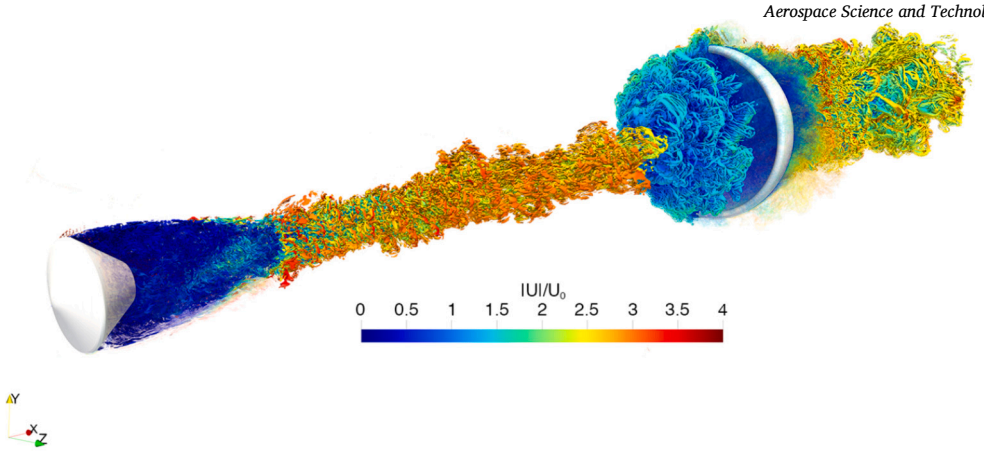

Fig. 2. Q-criterion 3D representation of the flow around the descent module and parachute using non-dimensional velocity magnitude. Vortical structures in the recirculation region of the capsule and in front of the canopy are set partially transparent to illustrate inner flow dynamics. (For interpretation of the colors in the figure(s), the reader is referred to the web version of this article.)

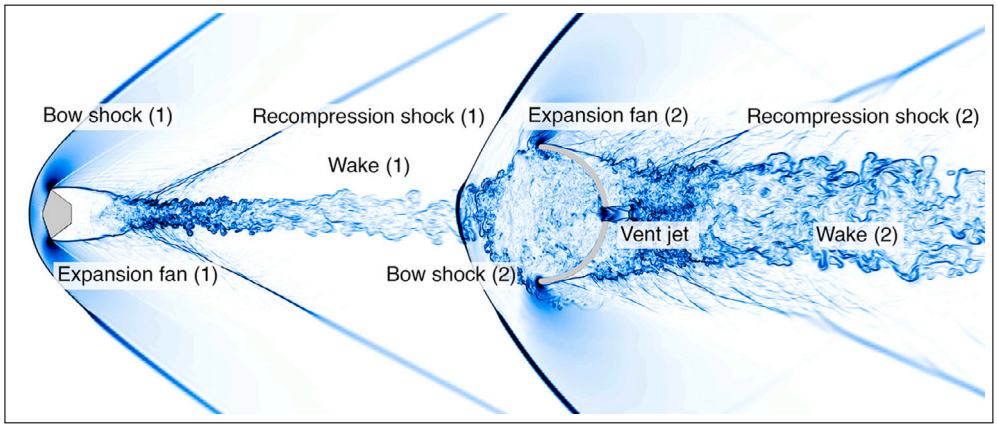

Fig. 3. Instantaneous contours of density gradient (numerical Schlieren) highlighting canonical flow regions and details; axial plane cross-section, full-domain view.

3. Results

3.1. Flow organization

The simulated flow field, as depicted in Fig. 2, reveals insights into the complex three-dimensional structures produced by the descent module and the parachute. Emerging flow features are presented with the use of the Q-Criterion technique to highlight turbulence structures in the wake of the module, as they move downstream towards the decelerator. At the position of the parachute bow shock, eddies from upstream exhibit an apparent increase in size, developing larger vortices as they pass through the compression discontinuity. This transition effect serves as the driving factor of the unsteady dynamics surrounding the decelerator in supersonic regimes. Contour colors represent the distribution of velocity magnitude: flow accelerates after the near-wake region, forming small and sharp recirculating patterns. As the flow encounters the shock, it bluntly slows down, generating numerous vortices that fill the canopy volume before flowing out from the sides.

Given the axial symmetry of the studied system, results can be furtherly visualized via the use of two-dimensional sections along the central plane of symmetry (i.e. axial plane). In Fig. 3 we employ numerical Schieleren visualization to distinguish canonical flow regions and shock systems produced by the present configuration. The flow field exhibits the formation of two distinct bow shocks, one in front of the capsule and the other in front of the parachute. The bow shock in front of the capsule remains steady. In contrast, the bow shock ahead of the parachute exhibits unsteadiness attributed to upstream turbulence generated by the entry module. This disturbance generates an oscillating behavior characteristic of the 'breathing' phenomenon. Further details are given in the next section and in Fig. 5.

At the capsule shoulder, the flow rapidly recirculates around its edge, transitioning to supersonic speed as it traverses the expansion fan generated from the sides of the axial symmetrical geometry. Close to the surface, the flow detaches and forms a stable turbulent wake. Outside the wake region, the flow tends to recover freestream conditions through the action of the recompression shock.

A similar scheme of structures can be observed beyond the canopy region, although the flow is noticeably more unstable, and turbulent flow extends further due to the larger dimension of the body. Due to the geometry of the shock wave of the parachute, the wake flow originating from the capsule spreads transversely, forming an expanding conical turbulent flux tube as it surrounds the volume occupied by the canopy. The incoming turbulence also experiences significant amplification beneath the canopy shape as it crosses the shock, resulting in the formation of larger recirculating patterns, as observed already in the previous representation.

This flow interacts with the counterflow emerging from the canopy, periodically generating discharges from the sides of the decelerator. These discharges recirculate around the lip and rapidly expand through the expansion fan, which forms an annulus shape around the circumference of the parachute. Free-shear layers develop in the outer surface of the canopy, where flow detaches and contributes to the formation of its large turbulent wake. Moving at the center, in the outflow through the parachute vent, a supersonic jet behavior is observed, with the flow reaching its absolute maximum velocity. This results in the formation of

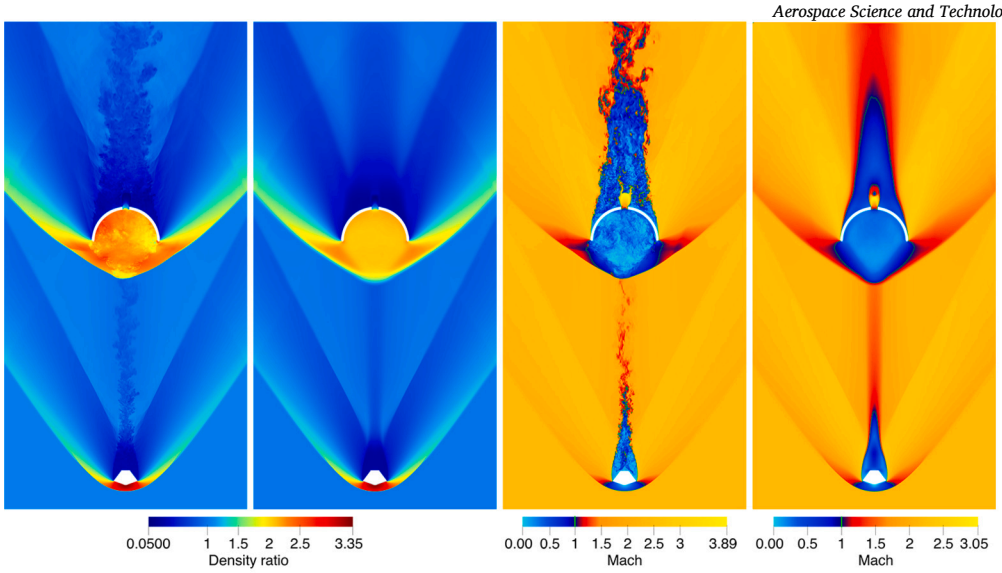

Fig. 4. Instantaneous and average contours of density ratio (left pair) and Mach number (right pair); axial plane cross-section, full-domain view.

a Mach disk within the recirculating region past the canopy. Additionally, flow outbursts from the vent contribute to further disturbance in the wake region of the parachute, generating eddy shocklets. Flow fluctuations inside the volume underlying the canopy surface couple also with the shape of the parachute bow shock, which waves strongly over time, displaying an asymmetric behavior due to the disruption caused by the recirculating flow from upstream.

More specific details related to the flow dynamics can be observed from Fig. 4, where instantaneous and averaged flow quantities are visualized through contour plots on the same cross sections.

Panels on the left display density ratio contours, depicting both instantaneous and average values, around the capsule and canopy. The density ratio contours highlight a stronger bow shock compression in the capsule compared to the parachute. This difference is attributed to the momentum deficit generated by the wake as it interacts with the canopy. Average flow field reveals the expected axial symmetrical recovery of flow features, including the shape of the parachute bow shock. However, the border of the bow shock appears smeared due to the unsteady standoff distance.

Panels on the right display Mach contours, both instantaneous and average. Subsonic regions are observed directly behind the bow shocks, particularly in the region concentrated around the central axis of the domain, where the shock is stronger due to its smaller inclination angle. The near-wake recirculation region of the capsule appears to be subsonic, while the far-wake transitions to sonic as it traverses the emerging recompression shock. Large subsonic vortical structures are generated inside the canopy volume, particularly in the area adjacent to the wake interaction and subsequently behind the decelerator. The highest velocity is attained by the flow exiting the vent, located right behind the Mach disk.

3.2. Parachute 'breathing'

In order to better evaluate the time-evolving dynamics related to the parachute, Fig. 5 proposes via panel view the progression of four instantaneous density ratio contour plots at different timesteps, from (a) at the top-left, to (d) bottom-right, directly showing the oscillation of the bow shock and the fluctuations of the flow state inside the canopy; plots are zoomed-in views of the central cross section.

Starting from the top-left panel (a) and moving to the top-right (b), we observe that the shock begins to move forward, indicating an increase in its relative speed with respect to the wake inflow velocity. As the shock moves forward and the standoff distance increases, a larger flux is permitted to escape from the canopy (c). The combined effect of volume expansion and density reduction within the canopy reduces the shock intensity and consequently the shock speed, causing the discontinuity motion to revert backwards. The reversion of shock motion, as depicted in the bottom-left panel (c), leads to a compression of the volume together with an increase of density. This compression restarts the cycle, as illustrated in the bottom-right panel (d).

In essence, the primary cause of this dynamics is attributed to the interaction between the wake turbulence beyond the capsule and the bow shock of the decelerator. These significant variations affect the equilibrium of the shock, resulting in a cyclic motion of the compression wave. The triggering factor lies in the velocity disparity between the incoming upstream flow and the velocity of the parachute bow shock. Wake perturbations induce oscillations around the average flow speed entering the shock, which can fluctuate to be either larger or smaller than the shock wave velocity. The velocity difference moves the shock, varying the standoff distance and thus the flow volume subtended by the canopy. This directly affects the flow state, which in turns alters the shock intensity and thus its speed, thereby sustaining the dynamics. This cyclic process continues indefinitely without reaching a steady-state due to the phase-shift between the wake inflow velocity and the shock speed.

Ultimately, the phase-shift between the shock and wake velocity can be attributed to the damping effect induced by the dimensions of the parachute, particularly its internal volume. This effect alters the response time of the bulk fluid state, which varies in accordance with the motion of the shock as the region where the flow converges changes.

3.3. Density and velocity fluctuations

We proceed by assessing the flow variability around the canopy region in terms of fluctuations, employing root mean squared (RMS) quantities related to the flow variables. On the left panel of Fig. 6, contours of the streamwise velocity fluctuations (root-mean square) highlight areas where flow oscillations are concentrated. The zone around the parachute bow position is evident, indicating that the unsteady shock induces axial fluctuations in the flow passing through. Notably, this area appears to be more spatially extended than the lateral regions of the shock wave. This suggests that this zone is subject to the largest amplitudes of oscillations due to the direct effect of the interacting turbulence from the wake. Past the shock, fluctuations persist along the sides of the expanding flux tube, delineating the interface (shear layer) between the flow deflected by the shock and the recirculation region within the shape of the canopy. Strong fluctuations streaks also emerge from the sides of

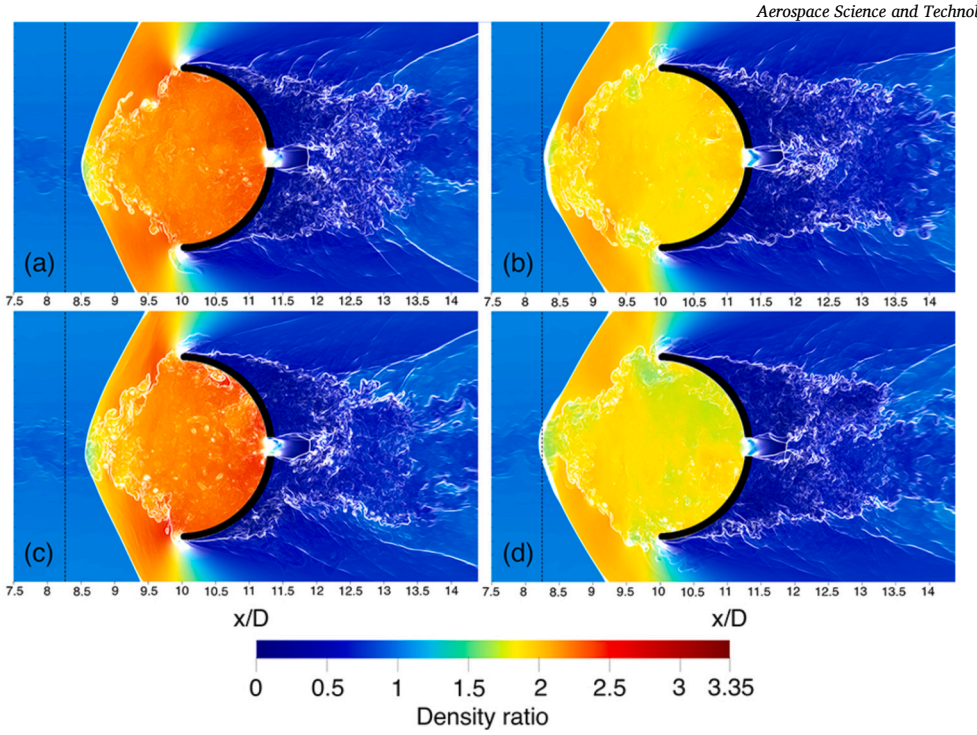

Fig. 5. Panel visualization showing 'breathing' cycle dynamics at different progressive timesteps from (a), top left, to (d), bottom right. Contours are enhanced using a mixed density ratio and numerical Schlieren representation; axial plane cross-section, full-domain view.

the canopy, indicating flow acceleration through lateral expansions and highlighting successive detachments. At the vent, the supersonic jet interacts with the surrounding recirculating subsonic flow; at the position of the Mach disk, the streamwise velocity fluctuations (u') reach their maximum. Subsequently, they persist along the wake.

The contours of density fluctuations (root-mean square) are instead depicted on the right panel, showing regions of the flow density field that undergo oscillations in time. Again, the canopy bow shock is prominently visible, indicating both the motion of the discontinuity and the width of its oscillation. The central shock position similarly shows the widest region of oscillation, attributed to perturbations in the wake causing ripples on the shock surface, which destabilize its shape and position. The magnitude of its fluctuations is slightly lower compared to the rest of the shock trace due to the larger distance from the body, resulting in a reduced compression effect. The trace of the frontal bow shock in the root-mean squared fields of both the streamwise velocity and the density ratio highlights the motion of the parachute shock wave, which, unlike the bow shock of the forebody that shows no fluctuations and thus no motion, directly shows the dynamic nature of the cyclic oscillation of the discontinuity of decelerator.

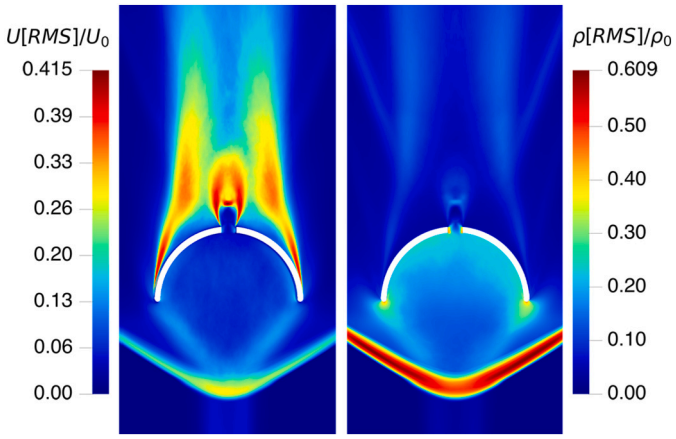

Fig. 6. Root-mean-square of streamwise velocity fluctuations (left) and root-mean-square density ratio fluctuations (right) contours; axial plane cross-section, zoomed-in view.

3.4. Near-parachute mean flow field

Further details on the flow overall recirculation dynamics are provided by streamline representation of the average flow fields. Fig. 7 depicts streamlines of the average flow Mach number, showing mean flow directions beyond the parachute bow shock.

Streamlines directions highlight a diverging subsonic region between the bow shock and the canopy. This region effectively forms an imaginary control volume where fluid enters from the central wake region and outflows at sonic condition laterally near the canopy skirt and through the vent, forming a spreading flux tube. Furthermore, streamlines directions emphasize the formation of two toroidal vortices, one within the canopy and another attached to its outer surface. The internal vortex is generated by the converging shape of the canopy, which redirects the flow toward the center and induces recirculation. It oscillates within the parachute internal volume due to the combined effect of the canopy hemispherical shape, which generates vorticity, and the turbulent flow supplied from the shock. Although it predominantly maintains its position beneath the canopy, as the vortex oscillates forward, it exerts pressure on the flow interface of the flux tube, thereby causing periodic discharge from the sides of the parachute and around the canopy. The vortex ring exhibits an unbalanced shape, cyclically expanding and contracting asymmetrically, which alternates the discharging behavior. This asymmetry reverses as one end begins to feed the other, and vice versa. Being this behavior related to the turbulence coming from upstream, the flow reestablish symmetry at statistically large timescales. The position of the internal vortex remains concentrated in the lower portion of the hemispherical canopy, accentuating fluctuations in this area, as also observed from the RMS contour plots in Fig. 6. This is in accordance with the behavior of parachute band/skirt collapse previously documented in the literature [25]. The general flow distribution represented by streamlines shows a slight deviation from an axial sym-

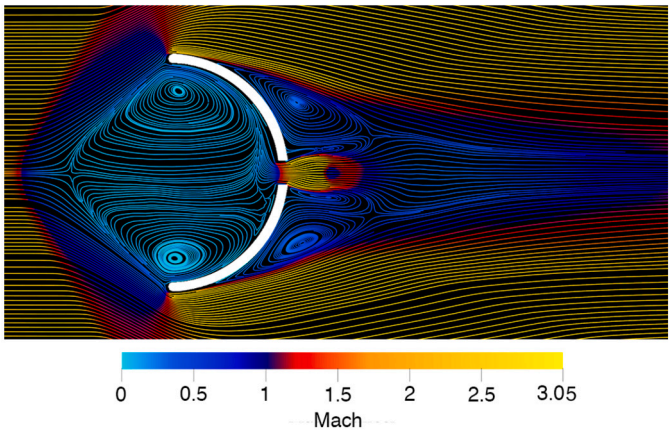

Fig. 7. Streamline visualization of the average Mach number flow field around the canopy (axial plane cross-section).

metrical configuration, despite adequate flow averaging. This deviation is attributed to the streamline seeding algorithm, which generates non-symmetrical flow traces due to constraints related to the uniform spacing of lines. However, the symmetrical positioning of the singularities of the vortices supports the presence of an underlying symmetrical flow distribution, reinforcing the expected behavior.

3.5. Parachute shock dynamics and performances

To better quantify the dynamics of the parachute bow shock, the time evolution of the standoff distance Δ/D was extracted by locally tracking the density gradients. The distance is provided at multiple transvserve position for the xz axial plane. In Fig. 8 distinct oscillations associated with the 'breathing' instability are visible for every selected transverse position ($z/D=-1$, $z/D=0$ and $z/D=1$). The position of the bow shock clearly follows a cyclic behavior at a low frequency, corresponding to the cycle shown in Fig. 5. When comparing the dynamics computed off-axis with those at $z/D=0$, we observe that the trends are similar and in phase. This suggests that the bow shock is also relatively axial symmetrical and oscillates rigidly forward and backward without significantly altering its general shape. The amplitudes of oscillations are also comparable due to the relative proximity of the probing positions to the axis, placing them closer to the wake region. This is consistent with the observations made in the contours of the fluctuating fields (Fig. 6). Very faint and limited high-frequency fluctuations are observed at $z/D=0$, indicating a source of disturbances related to the inflow of large turbulent structures from the wake. This can be observed from the underlying dashed black line, from which the solid line was derived through a filtering operation.

Performances of the decelerator are ultimately given in Fig. 9, where force coefficients produced by the parachute are plotted versus time, with the axial direction displayed on the left (C_X or in this case C_D given $\alpha=0°$) and the radial/transverse direction C_T on the right. Coefficients are computed using as reference surface the parachute nominal diameter D_0, which is given with $D_p/D_0=0.65$ [61]. Parachute drag coefficient exhibits oscillations which are primarily driven by a low-frequency content associated with the motion of the shock. Additionally, a higher frequency component is present, possibly linked to the partial or asymmetrical reshaping of the bow shock induced by wake turbulence. These oscillations are also evident in the dynamics of the standoff distance (Fig. 8), albeit in antiphase with the produced drag force. This finding aligns expectedly with the dynamics of the 'breathing' cycle illustrated previously in Fig. 5. A closer bow shock, resulting in a lower standoff distance, leads to an increase in the density and pressure field inside the parachute canopy. This, in turn, concordantly increases the drag force. Under the constant inflow condition ($Ma_\infty=2$ and $Re=10^6$), we calculate an average drag coefficient of $\overline{C_D}=0.58$, with oscillations about $\pm 15\%$ of mean value. This value is consistent with findings reported in the literature [24], where experimental evaluations of a rigid DGB parachute yielded similar results with the same trailing distance and a forebody-parachute ratio of $D/D_P=0.23$. The value is also consistent with the range reported by [61] for hemispherical parachutes. For comparison, parachute drag dynamics were also simulated for the same canopy under the same flight conditions, but without the presence of the forebody and the resulting wake disturbance (C_D^*). This side scenario showed instead a nearly constant drag coefficient, confirming once again that the incoming wake turbulence is the primary trigger of the instability. Polar plot of the transverse force coefficient $C_T=\sqrt{C_Y^2+C_Z^2}$ on the right panel shows fluctuations of similar frequency but smaller amplitudes compared to C_D. We observe concordantly that $\overline{C_Y}\approx 0$ and $\overline{C_Z}\approx 0$ while $\overline{C_T}=0.038$. Additionally, the polar plot illustrates the rotational and revolving dynamics of the lateral forces acting on the decelerator, complementing the oscillating drag behavior in the axial direction. This representation provides insight into a potential helicoidal motion around the wake of the forebody, a behavior commonly observed in parachutes during free flight.

4. Model of 'breathing'

4.1. Model formulation

Based on the assumption that the parachute bow shock instability is essentially dependent on perturbations from the upstream wake flow, as also supported by experimental evaluations [24], we develop a zero-dimensional model to replicate this behavior. In this framework the flow state within the canopy is considered spatially uniform, allowing its variation only in time. The model is based on the principles of mass and momentum balance, considering as known only the time dynamics of the inflow of the parachute induced by the turbulent wake. The underlying hypothesis implies that the shock in front of the canopy can be treated as normal, with a correction factor applied to account for the effective inflow area. A mathematical discussion of this approach is provided in the attached Appendix A. The purpose of the model is to yield semi-quantitative results for the quantities defining the unsteady dynamics of the parachute, specifically the flow state inside the canopy and the drag force produced by the decelerator. With the inflow streamwise velocity provided as input, the model produces density ratio as well as fluctuations in the drag force as outputs.

The driving mechanism of the model is rooted in the fundamental consideration that, in the absence of wake perturbation, the flow would attain an equilibrium state wherein the shock wave remains stationary, resulting in the inflow velocity being equal to the bow shock velocity. However, as illustrated in the previous section, the disparity in velocity between the incoming wake flow and the bow shock, forces the discontinuity either forward or backward, initiating the cycle. Changes in the control volume of the canopy, whether reductions or expansions, result in over or under-pressurisations, prompting turbulent flow inside the canopy to discharge or accumulate accordingly. The reliability and accuracy of the model are verified by comparison with results obtained from the present LES simulation. Firstly, equilibrium conditions, which corresponds also to the average flow field, are computed. Then, an input signal of inflow is provided to evaluate the dynamic response of the model.

Crucial to the model is the definition of the input signal, as its dynamics must replicate those associated with the turbulent wake to reproduce the same effects in the parachute response. Therefore, a proper analysis of the inflow wake is required to extract its overall spectrum and accordingly tune the model. The reference quantity selected to represent the wake dynamics is the streamwise Mach number, defined as $Ma_{sw}=u_1/\sqrt{\gamma RT}$. This choice is based on the direct involvement of u_1 in the wake-shock velocity deficit mechanism, which drives the 'breathing' instability in the current rigid configuration, as restated in the previous section. Wake spectrum analysis is conducted by examining flow

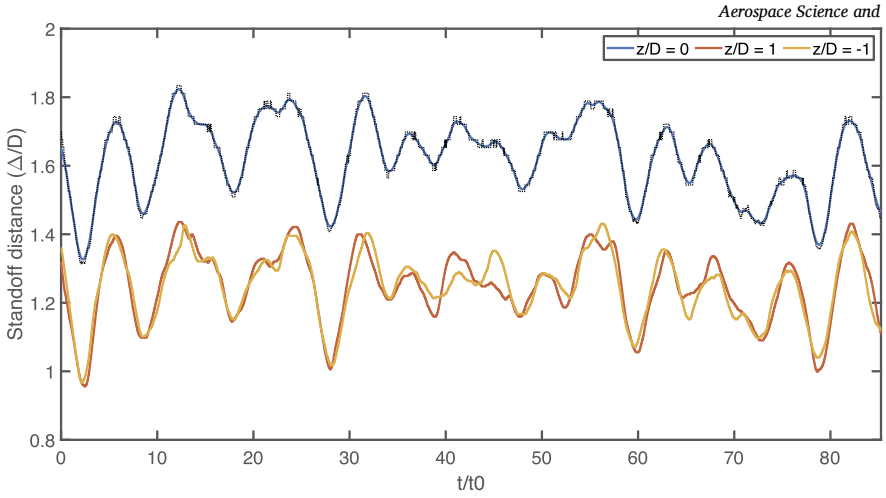

Fig. 8. Time dynamics of the parachute shock wave standoff distance measured at multiple transverse locations; dashed black line shows the unfiltered source signal.

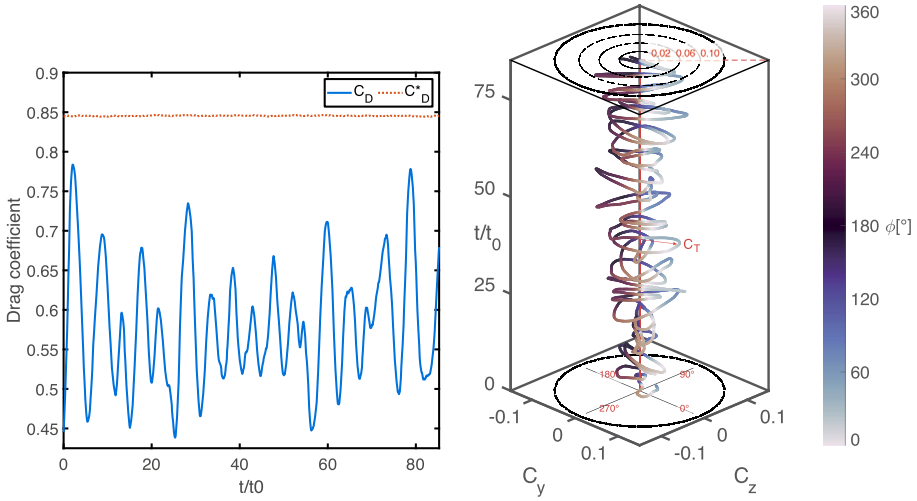

Fig. 9. Left: Time dynamics of the parachute axial force coefficient with ($C_D(t/t_0)$) and without the wake of the capsule ($C_D^*(t/t_0)$). Right: Polar plot of the parachute time-evolving transverse force coefficient $C_T(\theta, t/t_0)$.

fluctuations acquired from averaging five different cross sections in the yz plane spanning between $6.65 < x/D < 7.35$, which correspond to the far-wake region before the parachute bow shock. For each cross section, flow dynamics are recorded by averaging values of Ma_{sw} within a circle of radius $R_w = 0.3D$. The choice of R_w is based on the approximate width of the wake at that location. This approach yields a filtered signal of Ma_{sw} that represents the overall wake dynamics, effectively eliminating noisy high-frequency content attributed to low-energy, small chaotic recirculating patterns in the wake [36]. This is consistent with the quasi axial symmetric motion of the parachute bow shock, which resembles a rigid oscillation and is therefore more affected by the larger turbulence structures. The top panel of Fig. 10 illustrates the 3D setup of cross-sections in relation to their positions within the wake; Q-criterion applied to the capsule wake highlights turbulent structures included in the filtering region. The bottom left panel displays the Ma_{sw} signal obtained from this setup.

The Ma_{sw} time dependent signal is subsequently analyzed by extracting its spectrum using Welch's method, with three windows and an overlap factor of 50%. This method yields comparable results to a basic Discrete Fourier Transform (DFT) approach, but allows for an easier breakdown of the frequency components of the source signal. The bottom-right panel of Fig. 10 shows both the base DFT output and the results obtained using Welch's method.

We observe that most of the power of the signal, represented via power density, is concentrated in the low-frequency region, with $St < 0.210$; peaks are named from the strongest to the lowest in power. The highest and most distinct peak occurs at $St_1 = 0.040$, in a range between $0.036 < St < 0.057$ where multiple peaks tend to cluster; Welch's method locates an average common value. The lowest frequency detected is at $St_2 = 0.020$, with slightly half the power density of the former. Peaks at $St_3 = 0.093$ and $St_4 = 0.112$ appear with similar PSD. Additionally, within the low-frequency range ($St < 0.220$), three more peaks can be identified, each with about 20% of the largest power density: $St_5 = 0.132$, $St_6 = 0.153$ and $St_7 = 0.183$. Higher frequency contents are also present but are almost negligible due to the averaging process performed. Comparing the dynamics of the drag coefficient in Fig. 9 with $M_{sw}(t)$, we can observe that all the higher frequency contributions ($St > 0.210$), corresponding to small recirculations in the wake, do not propagate across the shock wave. These contributions appear to be damped and filtered by the shock-canopy system, so that only low-frequency disturbances are transmitted, with the bow shock effectively acting as a low-pass filter for the turbulence passing through.

Thus, by employing the frequency content found in the wake and assuming the inflow at the bow shock to be purely streamwise around its axis (within a circle of radius $R_w = 0.3$), we define the input for the model via a streamwise Mach number given by the expression:

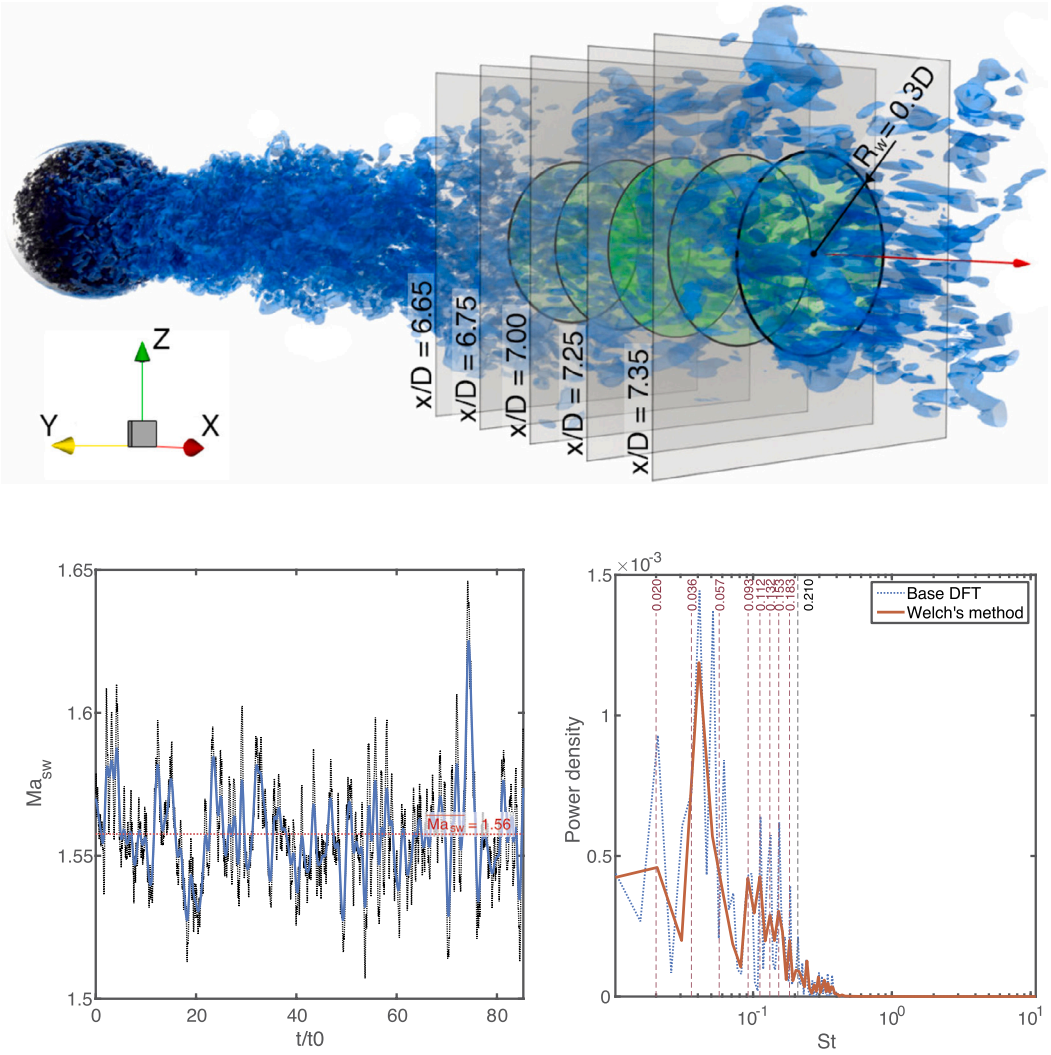

Fig. 10. Top: 3D representation of the wake averaging setup. Bottom: Left, time dynamics of the analyzed signal; the smoothed low-pass profile is highlighted in blue for clarity, with the red dashed line indicating the average Ma_{sw} value. Right: Frequency spectrum of the analyzed streamwise Mach number signal; the Strouhal number is computed as $St = f\,D/U_\infty$.

$$Ma_{sw}^{input} = \overline{Ma_{sw}} + \sum_i A_i sin\left(2\pi \frac{St_i U_\infty}{D} + \phi_i\right) \tag{7}$$

where $\overline{Ma_{sw}}$ is the average value of the inflow streamwise Mach number, A_i is the amplitude related to its i-th tone, St_i is the corresponding frequency and ϕ_i is its phase. From the analysis illustrated in Fig. 10, $\overline{Ma_{sw}} = 1.56$ and the tone parameters are progressively superimposed to obtain a more refined input signal to drive the model and replicate the parachute dynamics. A base signal composed of the first two frequencies in phase is given; from this base, a progressively more complex Ma_{sw} is obtained by adding the following higher frequency tones. To simplify the superimposition of the tones and average the effective phase shift between them, the added contributions are alternately summed in phase quadrature. By tuning the amplitude A_1 of the tone St_1 to 0.1, and considering the relationship between amplitude and power, by comparison A_2, A_3 and A_4 are round to 0.05 while A_5 and A_6 to 0.02; A_7 is instead set to 0.01. As previously stated, Equation (7) emphasizes the dynamic dependence of the model solely on the fluctuations originating from the upstream wake. The streamwise Mach number input is integrated into the model according to mass and momentum conservation principles, yielding results for the flow state within the canopy control volume and the resulting parachute drag.

4.2. Model results

Fig. 11 shows the model drag coefficient results compared to the present LES simulation. The output is evaluated as the streamwise Mach number signal used as an input is progressively made more complex by superimposing all the low-frequency tones that appeared from the spectrum analysis of the wake. For all six different input cases, the model yields the same average drag as the simulation, with an error of less than 1% in all cases (please refer to Table 3). The error slightly increases as higher frequency contents are added. However, regarding the dynamics and the amplitudes of oscillations of the parachute coefficient, significant improvement is observed as more tones are included in the error computed over $C_{D,RMS}$. The most crucial tone appears to be St_3 as it provides the largest relative improvement in the error when moving from St_{1-2} to St_{1-3} compared to the other cases. The error then further decreases, albeit at a slower pace, reaching a minimum of about 11%. Overall, considering the relative effect of reducing the error by adding content, the St_{1-4} configuration appears to be the most optimal in terms of the complexity of the input signal and the accuracy of the results. We expect that results could be further refined by conducting a more in-depth tuning campaign of the relative amplitudes and phase shifts between the extracted contents.

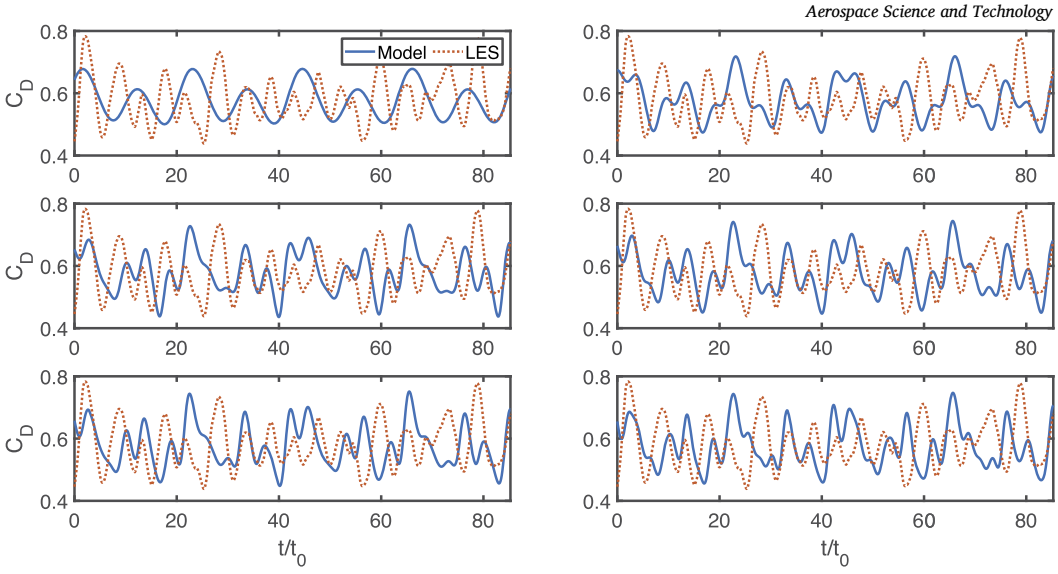

Fig. 11. Comparison between the parachute drag coefficient provided by the simulation and that obtained using the model. The model outputs are generated by progressively adding superimposed tones as input. From top left to bottom right: St_{1-2}, St_{1-3}, St_{1-4}, St_{1-5}, St_{1-6} and St_{1-7}.

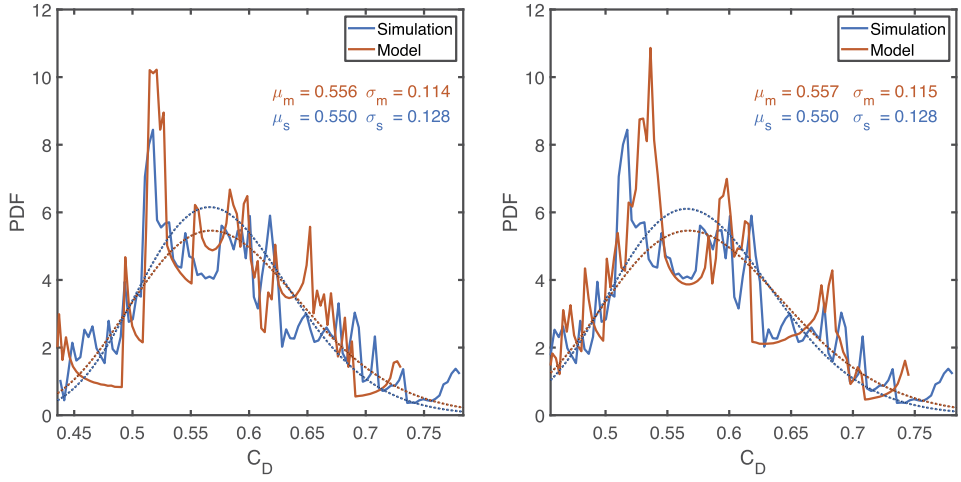

Fig. 12. Comparison of the probability density function of the drag coefficient obtained from the simulation and the model (left: S_{1-4}, right S_{1-7}). The corresponding fitted log normal probability distributions are shown for both cases, with the expected values μ_m, μ_s and deviation σ_m, σ_s reported accordingly.

Table 3
Model results.

	St_{1-2}	St_{1-3}	St_{1-4}	St_{1-5}	St_{1-6}	St_{1-7}
Error(%) over $\overline{C_D}$	0.753	0.743	0.724	0.740	0.745	0.766
Error(%) over $C_{D,RMS}$	28.90	20.31	13.35	12.38	11.47	10.93

To further evaluate the performance and confidence of the model output with the actual drag obtained with the LES simulation, Fig. 12 shows the probability-density function of the modeled drag (case St_{1-4} and St_{1-7}) compared with the actual one of the simulation.

It is apparent that the shape of the drag distribution obtained from the simulation is maintained in the dynamics reproduced by the model when employing a four-tone signal S_{1-4} as input (left panel of Fig. 12). Overall accuracy increases as further tones are added towards St_{1-7} (right panel). The modeled drag distribution particularly exhibits the same peak around 0.52 as shown by the simulation, closely following the log normal trend of the probability distribution. The distributions shown represent the closest fits to the data: the distribution shapes are comparable, given the similarity of the sources. Differences lie particularly in the right tail of the PDF pertaining to the highest values of C_D, corresponding to few sporadic peaks. This difference reduces as we move from S_{1-4} to S_{1-7}, suggesting that a progressively more refined input signal could improve the characterization of the highest drag peaks occurring occasionally.

5. Conclusions

This work discusses the high-fidelity, time-evolving simulation of a rigid parachute trailing behind a descent module in a supersonic flight regime, using LES and IBM techniques. The objective was to illustrate that the unsteady dynamics of the 'breathing' instability are primarily fluid-dependent, with the root of the phenomenon originating from the complex flow system given by the aerodynamic configuration, rather than being inherently linked to the structural flexibility of the decelerator.

The turbulent wake of the descent capsule interacts with the bow shock generated by the parachute, serving as the triggering factor for this phenomenon. It is the low-frequency components in the wake turbulence that initiate the instability and exert the most significant impact. To properly capture the dynamic turbulent structures of the flow field, the Large-Eddy Simulation approach is employed, along with energy-

preserving schemes that prevent excessive dissipation of flow unsteadiness. This enables us to observe the amplification of flow fluctuations as they pass through the shock discontinuity, which causes the main root of instability in the performance of the parachute.

These fluctuations induce local disturbances in the parachute shock state, altering the velocity of the bow shock and destabilizing its equilibrium with the upstream flow. As a result, the shock wave undergoes continuous cyclic motion without reaching a static equilibrium, primarily influenced by the turbulence within the wake, which either accelerates or decelerates the local propagation velocity of the shock. Since the velocity and motion of the shock are related to its intensity, periodic increases and decreases in intensity are observed as variations in the flow state inside the canopy volume, thereby affecting parachute performance. Introducing structural dynamics in the canopy and allowing deformations would potentially amplify this behavior over time, causing fluctuations in the projected parachute area and consequently altering the overall force generated. Connected to the periodic dynamics of the parachute are the cyclic discharges of flow from under the canopy volume. The simulation of the flow field inside and around the canopy highlights the formation of two separate toroidal vortical structures: a stronger one inside the canopy and a weaker one on the outer surface. The internal vortex produces periodic outflows related to the focusing of flow fluctuations on the lower portion of the canopy, which in turn feed the attached external vortex.

Based on the simulation results, a zero-dimensional model has been developed to capture the unsteady dynamics of the shock motion and predict the aerodynamic performance of the decelerator. The modeled dynamics are driven by an input signal created by superimposing pure tones extracted from the frequency analysis (DFT) of the capsule wake. This signal represents the streamwise Mach number of the flow interacting with the frontal bow shock of the parachute. These oscillations trigger the model, resulting in shock position oscillations that replicate both the physics of the phenomenon and the performance response of the decelerator, matching the dynamics observed in the simulation data. It is shown that the accuracy of the model results increases with the introduction of further complexity in the wake modeling. This is particularly evident when higher frequency tones are progressively superimposed.

This outcome provides valuable insights into the factors contributing to the unsteady responses of parachutes in supersonic regimes. By isolating structural and other multiphysics causes, we were able to clearly identify the root of the issue. This was supported by an analytical approach based exclusively on mass and momentum conservation principles.

Ultimately, the capabilities of the model are expected to be further extended to introduce more flexibility in the provision of input parameters, along with implementing the effects of structural deformations in the simulation process.

CRediT authorship contribution statement

Luca Placco: Writing – review & editing, Writing – original draft, Visualization, Methodology, Formal analysis, Data curation. **Giulio Soldati:** Writing – review & editing, Formal analysis, Data curation. **Matteo Bernardini:** Writing – review & editing, Software, Resources, Methodology. **Francesco Picano:** Writing – review & editing, Supervision, Project administration, Conceptualization.

Declaration of competing interest

The authors declare that they have no known competing financial interests or personal relationships that could have appeared to influence the work reported in this paper.

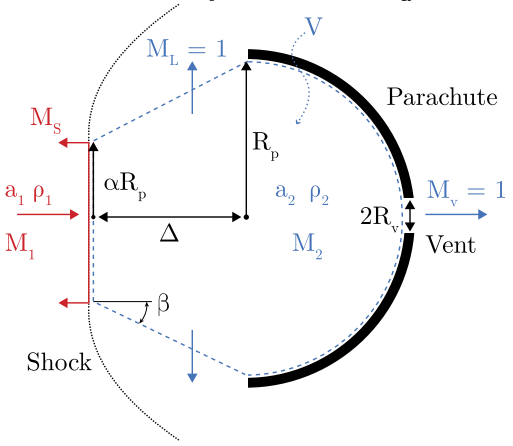

Fig. A.1. Scheme of the parachute area oscillation model.

Acknowledgements

We acknowledge that the results reported in this paper have been achieved using the ISCRA Research Infrastructure resource LEONARDO Booster based at CINECA, Casalecchio di Reno, Italy, under project Iscra-C no. **HP10C37F5U** FLAPDOME and Iscra-B no. **HP10BZ9ERG** MiSS-DOME. This research is supported by the Italian Space Agency (ASI, grant no. 2020-21-HH.0) in the framework of the ExoMars AMELIA experiment.

Appendix A. Model definition

Control volume $V(t)$ in Fig. A.1 is defined as:

$$V(t) = \frac{2}{3}\pi {R_p}^3 + \frac{\pi {R_p}^2}{3}(\alpha^2 + \alpha + 1)\Delta \tag{A.1}$$

which corresponds to the constant volume (hemisphere) inside the converging geometry representing the parachute canopy, and the time-varying volume (truncated cone) associated to the flux tube between the shock wave and the canopy. The parachute shock wave shape is approximated normal at the axis region as described in section 4.

R_p is the parachute radius as $D_p/2$. Shock standoff distance $\Delta(t)$ can be described by the following kinematic law: $\Delta(t) = \Delta_0 + (M_S - M_1)a_1 t$. Coefficient $\alpha(t)$ defines the time-varying effective inflow in the control volume and thus the dimension of the flux tube. It can be defined using the stand-off distance $\Delta(t)$ and the flux-tube angle β, which is fixed and acts as a model parameter; for the present work $\beta = 0.5\ rad$. From simple geometrical relations we can write: $\alpha(t) = (R_p - tan(\beta)\Delta)/R_p$. Surface $S_1(t) = \pi {R_p}^2 \alpha^2$ serves as an active time-varying surface where the inflow quantities are applied.

By taking the derivative with respect to time, we obtain the standoff distance rate-of-change:

$$\frac{d\Delta}{dt} \rightarrow \dot{\Delta} = (M_S - M_1)a_1 \tag{A.2}$$

Similarly, the control volume rate-of-change can be then defined as:

$$\frac{dV}{dt} = \pi {R_p}^2 \frac{d\Delta}{dt} = \pi {R_p}^2 (M_S - M_1)a_1 \tag{A.3}$$

A.1. Mass balance

$$\frac{d}{dt}\int_{V_c} \rho dV = 0 \tag{A.4}$$

We apply Reynolds transport theorem to (A.4) from [62]:

$$\underbrace{\frac{d}{dt}\int_V \rho dV}_{\rho \text{ variation in V (A.4.1)}} + \underbrace{\int_{\partial V} \rho(\vec{v}_r \cdot \vec{n}) dS}_{\rho \text{ fluxes (A.4.2)}} = 0$$

Replacing $\rho \rightarrow \rho_2 = const(\vec{X})$ in V, then (A.4.1) becomes:

$$\frac{d}{dt}\int_V \rho dV = \frac{d}{dt}(\rho_2 V) = V\frac{d\rho_2}{dt} + \rho_2 \frac{dV}{dt}$$

In (A.4.2) $\vec{v}_r$ represents the relative velocity of the interface of the control volume, which is $\vec{v}_r = \vec{v}$ everywhere except at the inlet position. In this case, considering the movement of the inlet interface given in equation (A.2) we can write:

$$v_r|_{inlet} = (M_1 a_1 - \dot{\Delta}) = (M_1 a_1 - (M_S - M_1)a_1) = (2M_1 - M_S)a_1$$

and expanding (A.4.2) with the corresponding local flow values we have:

$$\int_{\partial V} \rho(\vec{v}_r \cdot \vec{n}) dS = \underbrace{\pi {R_p}^2 \alpha^2 \rho_1 a_1 (2M_1 - M_S)}_{\text{inlet flux}} - \underbrace{(\pi {R_v}^2 \rho_2^* a_2^* + \rho_2^* a_2^* M_\Delta S_L)}_{\text{outlet flux}}$$

where $*$ indicates the flow quantity at the outflow position at sonic condition. In the outlet term R_v is the radius of the parachute vent as $D_v/2$ and S_L and M_Δ are respectively the truncated cone lateral surface and the flow component of M_L, which from geometrical considerations equal:

$$S_L = \pi R_p(\alpha + 1)\sqrt{\Delta^2 + {R_p}^2(1-\alpha)^2} \tag{A.5a}$$

$$M_\Delta = \frac{\Delta}{\sqrt{\Delta^2 + {R_p}^2(1-\alpha)^2}} \tag{A.5b}$$

With all the previous considerations, by taking into account equation (A.3) for the left-hand side, we divide by V and we get:

$$\frac{d\rho_2}{dt} = \frac{\pi {R_p}^2 \alpha^2 \rho_1 a_1 (2M_1 - M_S)}{V} - \frac{\pi {R_v}^2 \rho_2^* a_2^* + \rho_2^* a_2^* \Delta \pi R_p(\alpha+1)}{V} + - \frac{\rho_2 \pi {R_p}^2(\alpha^2 + \alpha + 1)(M_S - M_1)a_1}{3V} \tag{A.6}$$

We may rewrite with $P = \frac{\rho_2}{\rho_1}$ and $A = \frac{a_2^*}{a_1}$, obtaining:

$$\frac{dP}{dt} \rightarrow \dot{P} = \frac{\pi a_1}{V} \cdot \left[{R_p}^2 \alpha^2 (2M_1 - M_S) - \frac{\rho_2^*}{\rho_1}[{R_V}^2 A + \Delta R_p(\alpha+1)A] + - \frac{P {R_p}^2(\alpha^2 + \alpha + 1)(M_S - M_1)}{3} \right] \tag{A.7}$$

The system of equations is closed considering normal shock relations for $P = \frac{(\gamma+1)M_S^2}{2+(\gamma-1)M_S^2}$ where we obtain M_S as:

$$M_S = \sqrt{\frac{2P}{(\gamma+1) - P(\gamma-1)}} \tag{A.8}$$

From (A.2), (A.7) and (A.8) we may write the time-marching algorithm for P:

$$\begin{cases} \dot{P} = \frac{\pi a_1}{V} \cdot \left[{R_p}^2 \alpha^2 (2M_1 - M_S) - \frac{\rho_2^*}{\rho_1}[{R_V}^2 A + \Delta R_p(\alpha+1)A] + - \frac{P {R_p}^2(\alpha^2 + \alpha + 1)(M_S - M_1)}{3} \right] \\ M_S = \sqrt{\frac{2P}{(\gamma+1) - P(\gamma-1)}} \\ \dot{\Delta} = (M_s - M_1)a_1 \end{cases} \tag{A.9}$$

As stated in the model formulation section, the inflow Mach number is treated as an input and is therefore modeled with a sinusoidal function. For simplicity in the present example we consider only a single frequency content, with no phase shift, unlike to eq. (7).

$$M_1 := M_{sw}^{in} = \overline{Ma_{sw}} + A_{in} sin\left[2\pi\left(\frac{St_{in} U_\infty}{D}\right)t\right] \tag{A.10}$$

where $\overline{Ma_{sw}}$, A_{in} and St_{in} are obtained from the wake analysis, and represent the average oscillation of the inflow Mach number, similar to eq. (7). M_1 as M_{sw}^{in} stands as the only input quantity employed for the model.

Starting position for P, Δ and M_S is given by the equilibrium condition $\dot{P} = 0$, assuming $\alpha = 1$, which results in:

$$\begin{cases} M_S = \overline{Ma_{sw}} \\ P_e = \frac{(\gamma+1)\overline{Ma_{sw}}^2}{2 + (\gamma-1)\overline{Ma_{sw}}^2} \\ A_e = \sqrt{\frac{[2\gamma\overline{Ma_{sw}}^2 - (\gamma-1)][2 + (\gamma-1)\overline{Ma_{sw}}^2]}{(\gamma+1)^2\overline{Ma_{sw}}^2}} \\ \Delta_e = \frac{1}{2R_p}\left[\frac{2 + (\gamma-1)\overline{Ma_{sw}}^2}{(\gamma+1)\overline{Ma_{sw}}^2} {R_p}^2 \overline{Ma_{sw}} A_e - {R_V}^2\right] \end{cases} \tag{A.11}$$

A.2. Momentum balance

In order to model the forces generated by the parachute, momentum conservation principle is employed:

$$\vec{F_{ext}} = \frac{d}{dt}\int_{V_c} \rho \vec{v} dV \tag{A.12}$$

We apply Reynolds transport theorem to equation (A.12) on the same control volume $V(t)$:

$$\vec{F_{ext}} = \frac{d}{dt}\int_V \rho \vec{v} dV + \int_{\partial V} \rho \vec{v}(\vec{v}_r \cdot \vec{\mathbf{n}}) dS$$

Considering $\vec{F_{ext}} = \int_{\partial V} \vec{t} \cdot \vec{\mathbf{n}} dS$ where $\vec{t}$ is the tension applied to the control volume surface, we get:

$$\int_{\partial V} \vec{t} \cdot \vec{\mathbf{n}} dS = \frac{d}{dt}\int_V \rho \vec{v_r} dV + \int_{\partial V} \rho \vec{v}(\vec{v}_r \cdot \vec{\mathbf{n}}) dS \tag{A.13}$$

where

$$\int_{\partial V} \vec{t} \cdot \vec{\mathbf{n}} dS = \underbrace{\int_{\partial V_1} \vec{t} \cdot \vec{\mathbf{n}} dS}_{\text{inlet (A.13.1)}} + \underbrace{\int_{\partial V_2} \vec{t} \cdot \vec{\mathbf{n}} dS}_{\text{lateral flows (A.13.2)}} + \underbrace{\int_{\partial V_3} \vec{t} \cdot \vec{\mathbf{n}} dS}_{\text{canopy (A.13.3)}} + \underbrace{\int_{\partial V_4} \vec{t} \cdot \vec{\mathbf{n}} dS}_{\text{outlet (A.13.4)}}$$

Projecting equation (A.13) in the $\vec{\mathbf{x}}$ direction, we obtain that term (A.13.3) represents the drag force produced by the parachute. By neglecting viscous effects, $|\vec{t}| = p$ for terms (A.13.1), (A.13.2) and (A.13.4). For part (A.13.1), ∂V_1 defines the inflow area of the flux tube driven by α; for part (A.13.2), ∂V_2 represent the lateral surface of the truncated cone. Part (A.13.4) instead denotes with ∂V_4 the vent area S_v. Hence, we obtain:

$$\frac{d}{dt}\int_V \rho u dV + \int_{\partial V} \rho u(\vec{v}_r \cdot \vec{\mathbf{n}}) dS = -F_D + \int_{S_1} p dS - \int_{S_V} p dS + \int_{S_L} p dS$$

Left-hand side is expanded by solving the fluxes. As seen previously, the relative velocity of the control volume at S_1 is $\vec{v}_r = 2u_1 - u_s$. We obtain:

$$F_D = (2\rho_1 {u_1}^2 - \rho_1 u_1 u_s + p_1)S_1 +$$

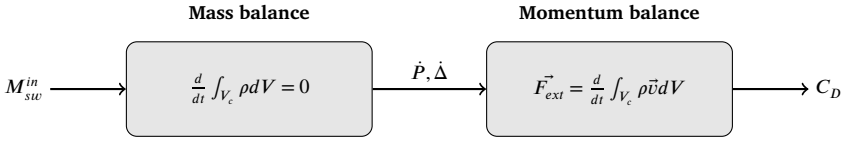

Fig. A.2. Block diagram of the model.

$$-(\rho_2^* u_2^{*2} + p_2^*)S_v + p_2^* S_L sin(\beta) - \frac{d}{dt}\int_V \rho u dV \quad \text{(A.14)}$$

where $*$ indicates the sonic state at outflow positions. We obtain $u_1 = M_1 a_1$ by definition and instead via Rankine-Hugoniot $u_2 = \frac{M_1 a_1}{P}$. From geometrical evaluations we derive $sin(\beta) = (1-\alpha)R_p / \sqrt{\Delta^2 + {R_p}^2(1-\alpha)^2}$.

Considering $\rho \to \rho_2 = const(\vec{X})$ and $u \to u_2 = const(\vec{X})$ in V, we may rewrite the derivative term in equation A.14 as:

$$\frac{d}{dt}\int_V \rho u dV = \frac{d}{dt}(\rho_2 u_2 V) = \underbrace{\rho_2 u_2 \frac{dV}{dt}}_{\text{term (A.14.1)}} + \underbrace{u_2 V \frac{d\rho_2}{dt}}_{\text{term (A.14.2)}} + \underbrace{\rho_2 V \frac{du_2}{dt}}_{\text{term (A.14.3)}} \quad \text{(A.15)}$$

Term (A.14.1) and (A.14.2) are treated using equation (A.1) and (A.6):

$$\rho_2 u_2 \frac{dV}{dt} = \rho_1 u_2 P[\pi {R_p}^2 (M_S - M_1)a_1] \quad \text{(A.16)}$$

$$u_2 V \frac{d\rho_2}{dt} = u_2 \rho_1 V \dot{P} \quad \text{(A.17)}$$

To solve term (A.14.3) we employ again Rankine-Hugoniot relations for u_2. Term (A.14.3) is then rewritten as:

$$\rho_2 V \frac{du_2}{dt} = \rho_2 a_1 V \frac{d}{dt}\left[\frac{M_1}{P}\right] = \frac{\rho_2 V a_1}{P}\left[M_1 \dot{P} + P\frac{dM_1}{dt}\right]$$

We can further expand the term in this particular case by taking the derivative of eq. (A.10) with respect to time:

$$\rho_2 V \frac{du_2}{dt} = \frac{\rho_1 a_1 V}{P}\left\{M_1 \dot{P} + 2P\pi S t_{in} A_{in} cos\left[2\pi\left(\frac{St_{in} U_\infty}{D}\right)t\right]\right\} \quad \text{(A.18)}$$

Combining equation (A.16), (A.17), (A.18) in equation (A.15), we obtain the parachute drag force from equation (A.14) as:

$$\begin{aligned} F_D = {} & (2\rho_1 {u_1}^2 - \rho_1 u_1 u_s + p_1)S_1 - (\rho_2^* u_2^{*2} + p_2^*)S_V + \\ & + p_2^* \pi R_p^2 (1-\alpha^2) - \rho_1 u_2 P[\pi {R_p}^2 (M_S - M_1)a_1] + \\ & - u_2 \rho_1 V \dot{P} - \rho_1 a_1 V\{M_1 \dot{P} + 2P\pi S t_{in} A_{in} cos[2\pi(St_{in} U_\infty / D)t]\} P^{-1} \end{aligned} \quad \text{(A.19)}$$

Drag coefficient is ultimately computed with:

$$C_D = \frac{8F_D}{\pi {D_0}^2 (M a_\infty a_\infty)^2} \quad \text{(A.20)}$$

where D_0 is the nominal diameter of the parachute. Block diagram in Figure (A.2) summarises the basic input-output structure of the model.

A.3. Model extension

Given the theoretical derivation of the model from first principles of physics and the relatively limited number of assumptions made, a natural extension of the model is anticipated and encouraged. Since the current formulation is specific to the present geometric configuration, further customization can be achieved by modifying the geometric characteristics associated with the employed parachute shape. In the context of the model derivation, this would translate into a modification of how the canopy control volume is primarily defined, including the geometrical porosity (i.e., the openings in the canopy of the parachute). A potential geometric extension could involve a disk-gap-band configuration: adapting the model to such a geometry would require replacing the straightforward hemispherical surface with the more complex, arbitrary geometry. Moreover, to account for the outflow through the gap area which is characteristic of that geometry, an additional term must be included in the outlet flux expression (A.4.2); this adjustment increases the effective surface where the flow discharges at sonic conditions from the canopy.

Regarding the extension of the physical basis of the model, incorporating the treatment of the structural porosity to account for the fabric nature of the decelerator could be considered. By implementing the Darcy-Forchheimer equation, using together the internal flow state within the canopy and estimating the external flow state through an average differential pressure would allow for a more refined evaluation of the flux balance in the canopy control volume. In this context, also introducing multiple control volumes to represent distinct flow areas inside and around the canopy could further enhance the accuracy of the model, ultimately yielding a more precise estimation of the drag coefficient.

A strong dependence of the model's accuracy was observed based on the treatment of its input parameters (i.e., eqs. (A.10) and (7)). Further wake analysis and an improved approach to modeling the incoming wake turbulence could enhance the accuracy of the predictions, potentially reducing discrepancies with experiments.

Table B.1
Summary of the validation campaign: comparison of the average drag coefficient with reference values.

Test case	Avg. drag coefficient	Exp. data	Error(%)
Mach 2, $Re = 10^6$	1.055	1.012 [63]	4.25
Mach 4, $Re = 10^6$	0.993	0.939 [63]	5.75
Mach 6, $Re = 10^6$	0.963	0.923 [64]	4.33

Appendix B. Validation of the software

The accuracy and reliability of the numerical solver STREAmS were assessed by conducting three Large-Eddy Simulations for a sphere in supersonic flow conditions at Mach numbers 2, 4, and 6; domain is discretised with a total of 14 million nodes. The Reynolds number for all cases was set to 10^6, and the specific heat ratio $\gamma = 1.4$. The computed average drag coefficient was compared with reference values from the literature ([63,64]) for the same flow conditions. The results showed good agreement, confirming the capability of the solver to accurately predict fluctuating aerodynamic forces in supersonic regimes. This validation provides additional confidence in the robustness of STREAmS when applied to unsteady, compressible flows relevant to the present study. See Table B.1 and Fig. B.1.

Data availability

Data will be made available on request.

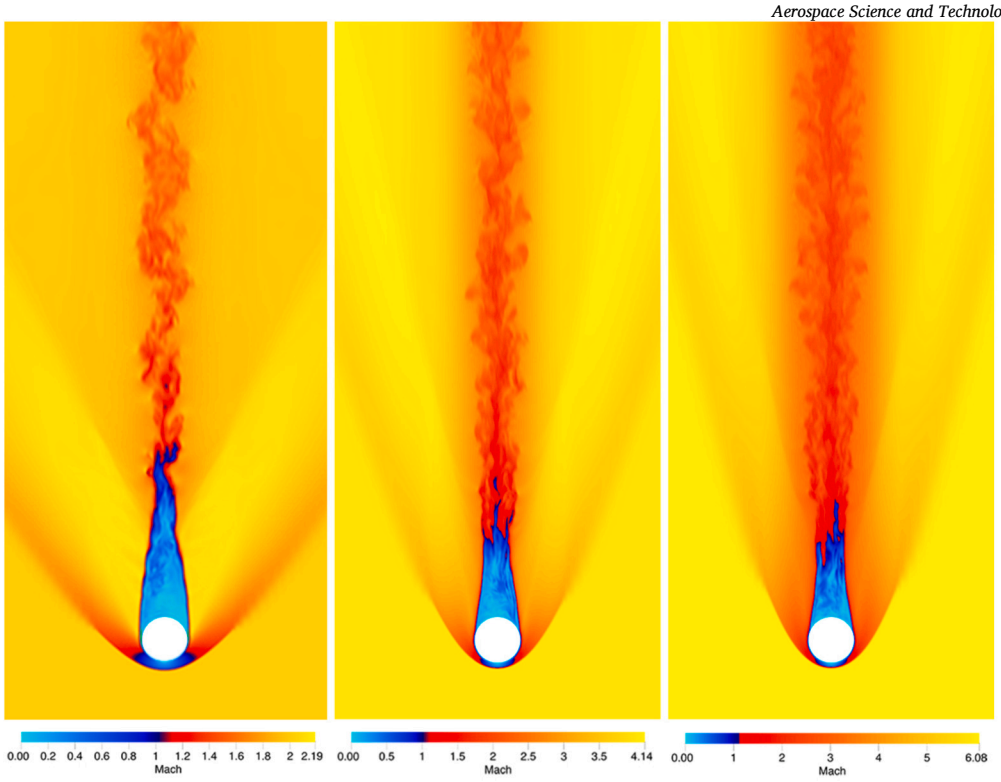

Fig. B.1. Instantaneous contours of a sphere in supersonic flow at different Mach numbers (2: left, 4: center, 6: right); axial plane cross-section, full-domain view.

References

[1] R.A. Meyer, Wind tunnel investigation of conventional types of parachute canopies in supersonic flow, 1958, WADC 58-532.
[2] Anonymous, X-7A supersonic ramjet test vehicle parachute recovery system, section I - pretest and test program, section II - recovery system, 1955, WADC 55-162.
[3] J.D. Maynard, Aerodynamic characteristics of parachutes at Mach numbers from 1.6 to 3, 1961, NASA TN D-752.
[4] N. Charczenko, T. McShera, Aerodynamic characteristics of towed cones used as decelerators at Mach numbers from 1.57 to 4.65, 1961, NASA TN D-994.
[5] T. McShera, Aerodynamic characteristics of towed cones used as decelerators at Mach numbers from 1.57 to 4.65, 1963, NASA TN D-1601.
[6] C. Eckstrom, Development and testing of the Disk-Gap-Band parachute used for low dynamic pressure applications at ejection altitudes at or above 200,000 feet, 1966, NASA CR 502.
[7] J.J. McFall, H. Murrow, Parachute testing at altitudes between 30 and 90 kilometers, in: Aerodynamic Deceleration Systems Conference, 1966.
[8] J.J. McFall, Some test results from the NASA Planetary Entry Parachute Program, J. Spacecr. Rockets 6 (1969) 621–623.
[9] R. Moog, Balloon launched Viking decelerator test program, 1973, NASA TR-3720359.
[10] R. Ross, F. Nebiker, Survey of aerodynamic deceleration systems, in: Third AIAA Annual Meeting, 1966, pp. 66–988.
[11] J. Hussong, R. Lau, The Viking Mars lander decelerator system, 1970, AEDC-TR-72-78.
[12] D.E.A. Reichenau, Aerodynamic characteristics of Disk-Gap-Band parachutes in the wake of Viking entry forebodies at Mach numbers from 0.2 to 2.6, 1971, AIAA 70-1162.
[13] S. Steinberg, P. Siemers III, R. Slayman, Development of the Viking parachute configuration by wind-tunnel investigation, J. Spacecr. 11 (1974) 101–107.
[14] R.N. Ingoldby, et al., Entry data analysis for Viking Landers 1 and 2 - final report, 1976, NASA CR-159388.
[15] P.C. Klimas, Internal parachute flows, J. Aircr. 9 (1972) 313–314.
[16] P.C. Klimas, Inflating parachute differential pressures, J. Aircr. 16 (1979) 861.
[17] J.H. Strickland, H. Higuchi, Parachute aerodynamics - an assessment of prediction capability, J. Aircr. 33 (1996) 241–252.
[18] D. Barnette, Preliminary numerical simulations for parachutes using a Navier-Stokes solver on a zoned grid, 1991, AIAA-91-0876.
[19] K.R. Stein, R.J. Benney, E.C. Steeves, A computational model that couples aerodynamic and structural dynamic behavior of parachutes during the opening process, 1993, NATICK/TR-93/029.
[20] E. Haug, D. Lasry, P. Kermel, Dynamic simulation of industrial membranes including their interaction with surrounding media, in: Third International Symposium of the SBF 230 Evolution of Natural Structures, 1994.
[21] J. Nelsen, Computational fluid dynamics studies of solid and ribbon 12-gore parachute canopies in subsonic and supersonic flow, 1995, AIAA-95-1558.
[22] J. Sahu, C. Gene, R. Benney, 3-D parachute descent analysis using coupled CFD and structural codes, 1995, AIAA-95-1580.
[23] J. Cruz, J. Lingard, Aerodynamic decelerators for planetary exploration: Past, present, and future, 2006, AIAA 2006-6792.
[24] A. Sengupta, A. Steltzner, A. Witkowski, G. Candler, C. Pantano, Findings from the supersonic qualification program of the Mars Science Laboratory parachute system, 2009, AIAA 2009-2900.
[25] M. Barnhardt, T. Drayna, I. Nompelis, G. Candler, W. Garrard, Detached Eddy Simulations of the MSL parachute at supersonic conditions, 2007, AIAA 2007-2529.
[26] K. Karagiozis, R. Komati, F. Cirak, C. Pantano, A computational study of supersonic Disk-Gap-Band parachutes using Large-Eddy Simulation coupled to a structural membrane, J. Fluids Struct. 27 (2011) 175–192.
[27] J. Lingard, M. Darley, Simulation of parachute fluid structure interaction in supersonic flow, 2005, AIAA 2005-1607.
[28] J. Lingard, M. Darley, J. Underwood, Simulation of Mars supersonic parachute performance and dynamics, 2007, AIAA 2007-2507.
[29] Y. Kim, P. Charles, 3-D parachute simulation by the immersed boundary method, Comput. Fluids 38 (2009) 1080–1090.
[30] K. Takizawa, T. Tezduyar, Computational methods for parachute fluid–structure interactions, Arch. Comput. Methods 19 (2012) 125–169.
[31] K. Takizawa, T. Tezduyar, Porosity models and computational methods for compressible-flow aerodynamics of parachutes with geometric porosity, Math. Models Methods 27 (2017) 771–806.
[32] X. Gao, Q. Zhang, Q. Tang, Numerical modelling of Mars supersonic Disk-Gap-Band parachute inflation, Adv. Space Res. 57 (2016) 2259–2272.
[33] S. Muppidi, C. O'Farrell, C. Tanner, J.W.V. Norman, I.G. Clark, Modeling and flight performance of supersonic Disk-Gap-Band parachutes in slender body wakes, in: 2018 Atmospheric Flight Mechanics Conference, 2018.
[34] B. Sonneveldt, I. Clark, C. O'Farrell, Summary of the Advanced Supersonic Parachute Inflation Research Experiments (ASPIRE) Sounding Rocket Tests with a Disk-Gap-Band Parachute, AIAA Aviation, 2019, Forum (2019).
[35] C. O'Farrell, S. Muppidi, J.M. Brock, J.W. Van Norman, I.G. Clark, Development of models for Disk-Gap-Band parachutes deployed supersonically in the wake of a slender body, in: 2017 IEEE Aerospace Conference, 2017.
[36] L. Placco, M. Cogo, M. Bernardini, A. Aboudan, F. Ferri, F. Picano, Large-eddy simulation of the unsteady supersonic flow around a Mars entry capsule at different angles of attack, Aerosp. Sci. Technol. 143 (2023) 108709.
[37] H. Yu, C. Pantano, F. Cirak, Large-eddy simulation of flow over deformable parachutes using immersed boundary and adaptive mesh, in: AIAA Scitech 2019 Forum, 2019.
[38] H. Yu, C. Pantano, F. Cirak, An immersed boundary method with implicit body force for compressible viscous flow, J. Comput. Phys. 459 (2022) 111125.

[39] D.Z. Huang, P. Avery, C. Farhat, J. Rabinovitch, Modeling, simulation and validation of supersonic parachute inflation dynamics during Mars landing, in: AIAA Scitech 2020, 2020.
[40] J. Boustani, G. Anugrah, M.F. Barad, C.C. Kiris, C. Brehm, A numerical investigation of parachute deployment in supersonic flow, in: AIAA Scitech 2020 Forum, 2020.
[41] J. Boustani, M.F. Barad, C.C. Kiris, C. Brehm, An immersed interface methodology for simulating supersonic spacecraft parachutes with fluid–structure interaction, J. Fluids Struct. 114 (2022) 103742.
[42] P. Avery, D.Z. Huang, W. He, J. Ehlers, A. Derkevorkian, C. Farhat, A computationally tractable framework for nonlinear dynamic multiscale modeling of membrane woven fabrics, Int. J. Numer. Methods Eng. 122 (2021) 2598–2625.
[43] D.Z. Huang, P. Avery, C. Farhat, An embedded boundary approach for resolving the contribution of cable subsystems to fully coupled fluid-structure interaction, Numer. Methods Eng. 122 (2021) 5409–5429.
[44] J. Rabinovitch, F. As'ad, F.P. Avery, C. Farhat, N. Ataei, M. Lobbia, Update: modeling supersonic parachute inflations for Mars spacecraft, in: Aerodynamic Decelerator Systems Technology Conferences, 2022.
[45] J. Boustani, F. Cadieux, G. Kenway, M.F. Barad, C.C. Kiris, C. Brehm, Fluid-structure interaction simulations of the ASPIRE SR01 supersonic parachute flight test, Aerosp. Sci. Technol. 126 (2022) 107596.
[46] C. O'Farrell, E.A. Leylek, M.A. Lobbia, K.J. Siegel, ASPIRE2: the Mars sample retrieval lander's supersonic parachute test program, in: 2023 IEEE Aerospace Conference, 2023, pp. 1–9.
[47] F. Nicoud, F. Ducros, Subgrid-scale stress modelling based on the square of the velocity gradient tensor, Flow Turbul. Combust. 62 (1999) 183–200.
[48] G. Erlebacher, M.Y. Hussaini, C.G. Speziale, T.A. Zang, Toward the large-eddy simulation of compressible turbulent flows, J. Fluid Mech. 238 (1992) 155–185.
[49] A. Yoshizawa, Statistical theory for compressible turbulent shear flows, with the application to subgrid modeling, Phys. Fluids 29 (1986) 2152–2164.
[50] C. Wollblad, L. Davidson, L.-E. Eriksson, Large eddy simulation of transonic flow with shock wave/turbulent boundary layer interaction, AIAA J. 44 (2006) 2340–2353.
[51] M. Bernardini, D. Modesti, F. Salvadore, S. Pirozzoli, STREAmS: a high-fidelity accelerated solver for direct numerical simulation of compressible turbulent flows, Comput. Phys. Commun. 263 (2021) 107906.
[52] M. Bernardini, D. Modesti, F. Salvadore, S. Sathyanarayana, G. Della Posta, S. Pirozzoli, STREAmS-2.0: supersonic turbulent accelerated Navier-Stokes solver version 2.0, Comput. Phys. Commun. 285 (2023) 108644.
[53] F. Ducros, V. Ferrand, F. Nicoud, C. Weber, D. Darracq, C. Gacherieu, T. Poinsot, Large-eddy simulation of the shock/turbulence interaction, J. Comput. Phys. 152 (1999) 517–549.
[54] F. De Vanna, A. Benato, F. Picano, E. Benini, High-order conservative formulation of viscous terms for variable viscosity flows, Acta Mech. 232 (2021) 2115–2133.
[55] A. Piquet, O. Roussel, A. Hadjadj, A comparative study of Brinkman penalization and direct-forcing immersed boundary methods for compressible viscous flows, Comput. Fluids 136 (2016) 272–284.
[56] F. De Vanna, F. Picano, E. Benini, A sharp-interface immersed boundary method for moving objects in compressible viscous flows, Comput. Fluids 201 (2020) 104415.
[57] M. Cogo, F. Salvadore, F. Picano, M. Bernardini, Direct numerical simulation of supersonic and hypersonic turbulent boundary layers at moderate-high Reynolds numbers and isothermal wall condition, J. Fluid Mech. 945 (2022) A30.
[58] M. Bernardini, G. Della Posta, F. Salvadore, E. Martelli, Unsteadiness characterisation of shock wave/turbulent boundary-layer interaction at moderate Reynolds number, J. Fluid Mech. 954 (2023) A43.
[59] G.D. Posta, E. Martelli, F. Salvadore, M. Bernardini, High-fidelity simulations of microramp-controlled shock wave/boundary layer interaction, 2024.
[60] A. Aboudan, G. Colombatti, C. Bettanini, F. Ferri, S. Lewis, B. Van Hove, O. Karatekin, S. Debei, ExoMars 2016 Schiaparelli module trajectory and atmospheric profiles reconstruction, Space Sci. Rev. 214 (2018) 1572–9672.
[61] T.W. Knacke, Parachute Recovery Systems Design Manual, 1991, NWC TP 6575.
[62] F.M. White, Fluid Mechanics, 7th ed., McGraw-Hill, 2011.
[63] A. Bailey, J. Hiatt, Sphere drag coefficients for a broad range of Mach and Reynolds numbers, 1972, AIAA-10(11)-1436–1440.
[64] J.D. Anderson, Fundamentals of Aerodynamics, 6th ed., McGraw-Hill, 2017.